

Regulation of the phase transition temperature and hysteresis width by changing the composition of $\text{Eu}_{1-x}\text{La}_x\text{Fe}_3(\text{BO}_3)_4$ solid solution


K. N. Boldyrev^{1,*}, V. M. Burlakov², I. A. Gudim³, S. Yu. Gavrilkin⁴, and M. N. Popova¹

¹*Institute of Spectroscopy, Russian Academy of Sciences, 108840 Troitsk, Moscow, Russia*

²*Linacre College, University of Oxford, St Cross Road, Oxford OX1 3JA, United Kingdom*

³*Kirensky Institute of Physics, Siberian Branch of RAS, 660036 Krasnoyarsk, Russia*

⁴*Lebedev Physical Institute, Russian Academy of Sciences, 119991 Moscow, Russia*

 (Received 19 April 2021; revised 11 August 2021; accepted 14 September 2021; published 29 September 2021)

A detailed study of the structural phase transition in $\text{Eu}_{1-x}\text{La}_x\text{Fe}_3(\text{BO}_3)_4$ mixed crystals as a function of composition is reported. By analyzing a frequency shift of an electronic f - f transition in high-resolution optical spectra of Eu^{3+} ions, we detected a decrease in the phase transition temperature T_s from 87.05 to 12.2 K (upon cooling) and a simultaneous increase in thermal hysteresis ΔT_s from 0.29 to 4.7 K with increasing x from $x = 0$ to $x = 0.12$. A rectangular hysteresis loop was observed. The experimental $T_s(x)$ and $\Delta T_s(x)$ dependences are described within the developed analytical model utilizing linear decrease in T_s with x and treating the increase in ΔT_s in terms of the impurity-related decrease in the interaction between some local order parameters. We argue that $R_{1-x}R'_x\text{Fe}_3(\text{BO}_3)_4$ solid solutions, where R and R' are different rare-earth elements, can be used to implement optical storage devices and switches operating at any chosen temperature between 0 and 450 K. It is found that the changes in the composition and, correspondingly, structural phase transition parameters do not affect the magnetic phase transformation. $\text{Eu}_{0.88}\text{La}_{0.12}\text{Fe}_3(\text{BO}_3)_4$ demonstrates the structural phase transition at about 12 K, well below the Néel temperature $T_N = 32$ K.

DOI: [10.1103/PhysRevMaterials.5.094414](https://doi.org/10.1103/PhysRevMaterials.5.094414)

I. INTRODUCTION

Rare-earth (RE) iron borates $R\text{Fe}_3(\text{BO}_3)_4$ belong to a large family of functional RE borates $RM_3(\text{BO}_3)_4$ ($R = \text{La}, \text{Pr}\text{--}\text{Er}, \text{Y}; M = \text{Al}, \text{Ga}, \text{Sc}, \text{Fe}, \text{Cr}$) with the structural type of the natural mineral huntite [1,2]. The compounds of this family crystallize in the noncentrosymmetric trigonal space group $R\bar{3}2$ and incorporate helical chains of the MO_6 octahedra running along the c axis. The chains are interconnected by the isolated RO_6 distorted prisms and BO_3 groups. These materials possess useful physical properties such as high optical nonlinearity [3–5], low RE luminescence quenching rate even in concentrated materials (because different RE ions have no common neighboring oxygen ions) [5,6], and multiferroicity [7–13] that, together with excellent physical characteristics and chemical stability, give them a vast application potential (see, e.g., Refs. [4,12–16], and references therein).

Containing a magnetic d ion (Fe^{3+}) in the structure, iron borates undergo magnetic phase transitions. The strongest magnetic interaction is the Fe-Fe exchange; then the R -Fe interactions follow, the R - R ones being negligible. The Fe-Fe exchange interaction causes an antiferromagnetic ordering at a temperature T_N , which depends on the average linearly on the ionic radius r of the R^{3+} ion and covers the range be-

tween 23 K for $\text{LaFe}_3(\text{BO}_3)_4$ [17] and 40 K for $\text{TbFe}_3(\text{BO}_3)_4$ [17–19]. The lattice constants and, consequently, the interatomic distances increase with increasing r , which decreases the Fe-Fe exchange interactions and decreases T_N . The RE subsystem becomes magnetically polarized below T_N via the R -Fe exchange interaction and, in turn, imposes a particular type of magnetic structure on the almost isotropic Fe subsystem [20,21]. Either an easy-axis ($R = \text{Pr}, \text{Tb}, \text{Dy}$) or an easy-plane ($R = \text{Nd}, \text{Sm}, \text{Eu}, \text{Gd}, \text{Ho}, \text{Er}, \text{and Y}$) magnetic structure is realized in $R\text{Fe}_3(\text{BO}_3)_4$ compounds, depending on a single-ion magnetic anisotropy of the R^{3+} ion [20,21].

A distinctive feature of the iron borates is a structural phase transition (PT). It was studied earlier by specific heat [17,22], Raman scattering [22,23], and infrared (IR) reflection [19] measurements. A strong, very narrow peak in the temperature dependence of specific heat [17,22] and an abrupt appearance of new Raman [22,23] and IR [19] modes at T_s exhibiting a hysteretic behavior of intensities [22,23] indicated the first-order character of the phase transition. However, a strong hardening of the lowest-frequency and the most intense new Raman mode upon lowering the temperature below T_s was typical for soft modes that announce a second-order structural phase transition [22,23]. Thus, the structural PT in RE iron borates possesses properties characteristic of both the first- and second-order PTs.

This PT is observed in the compounds containing the R^{3+} ions with the ionic radius r smaller than that of Sm^{3+} , and the PT temperature T_s scales linearly with r [17] covering the range between 0 and ~ 450 K. Below T_s , the structure is described by the also trigonal but less symmetric space group

*Present address: Dr. Kirill Boldyrev, Institute of Spectroscopy RAS, 5 Fyzicheskaya Str., 108840 Troitsk, Moscow, Russia; kn.boldyrev@gmail.com

$P3_121$ [2,23]. The structural peculiarities of both phases are described in detail in Refs. [2,24,25]. In particular, the R^{3+} ions occupy a single site in both phases, with the $D_3(C_2)$ point symmetry group in the high-temperature $R32$ (low-temperature $P3_121$) structural phase [2].

Dielectric and optical properties of RE iron borates undergo an abrupt change at T_s [19,22,23,26], which allows using these materials in various types of switches. The first reported data about T_s were obtained for powder samples prepared in the oxide systems by solid-state synthesis [17]. Subsequent studies on single crystals grown by the solution-melt technique using Bi-containing flux revealed markedly lower T_s for all studied $RFe_3(BO_3)_4$ samples, namely, 370 [24], 360 [25,27], 285 [28], 200 [19], 156 [22], and 58 K [29] in contrast to 445, 427, 340, 241, 174, and 88 K [17] for powder samples with $R = Y, Ho, Dy, Tb, Gd,$ and Eu , respectively. We hypothesized (see Refs. [19,27,29]) that the reason for such lowering of T_s is the incorporation of “large” Bi^{3+} ions from the flux into positions of R^{3+} ions in the crystal; and the concentration of Bi impurity in the crystal was estimated as $5 \pm 1\%$ for $EuFe_3(BO_3)_4$ [29] using the $T_s(r)$ dependence from Ref. [17] and the data on ionic radii [30]. A thorough x-ray diffraction study of yttrium [24] and holmium [25] iron borate crystals grown from a Bi-containing flux has established the composition as $(Y_{0.95}Bi_{0.05})Fe_3(BO_3)_4$ and $(Ho_{0.96}Bi_{0.04})Fe_3(BO_3)_4$, respectively, and confirmed our hypothesis and estimate. It is possible to avoid the incorporation of the flux elements into a crystal by using the Li_2WO_4 -based flux. While Bi^{3+} from the $Bi_2Mo_3O_{12}$ flux has the same charge state as the R^{3+} ion and a relatively close ionic radius [$r(Bi^{3+}) = 1.03 \text{ \AA}$, $r(La^{3+}) = 1.032 \text{ \AA}$, $r(Eu^{3+}) = 0.947 \text{ \AA}$], Li^+ differs greatly from both Eu^{3+} and Fe^{3+} in these parameters [$r(Li^+) = 0.76 \text{ \AA}$, $r(Fe^{3+}) = 0.55 \text{ \AA}$] and does not enter the crystal lattice. This is confirmed by the fact that the $Eu_{0.95}La_{0.05}Fe_3(BO_3)_4$ crystal grown with the Li_2WO_4 flux demonstrated the same $T_s = 58 \text{ K}$ as $Eu_{0.95}Bi_{0.05}Fe_3(BO_3)_4$ crystals [$EuFe_3(BO_3)_4$ grown with the $Bi_2Mo_3O_{12}$ flux] [29].

These results suggest that the temperature T_s of the structural PT in mixed iron borate crystals $R_{1-x}R'_xFe_3(BO_3)_4$, where R and R' are different RE elements, can be tuned linearly with x by varying the crystal composition x . In such way it would be possible to create switches as well as optical storage devices functioning at any chosen temperature between 0 and 450 K. At present, PT between amorphous and crystalline phases of a material such as the chalcogenide $Ge_2Sb_2Te_5$ is widely used in optical information technologies (DVD, CD-ROM, and so on; see, e.g., [31]). An optical memory with laser recording and reading, based on PT at $T_s \approx 130 \text{ K}$ between crystalline phases of gallium nanoparticles, has been demonstrated [32,33]. A search for new materials remains relevant, in particular, with T_s in the range of helium temperatures, where the majority of optical quantum technologies devices operate.

The main questions concerning the mixed $R_{1-x}R'_xFe_3(BO_3)_4$ crystals, which are important for applications, are (i) How sharp is the transition in the mixed crystals, and (ii) what is the value of a thermal hysteresis

ΔT_s . Here, we chose the $Eu_{1-x}La_xFe_3(BO_3)_4$ mixed system, in which $EuFe_3(BO_3)_4$ has the lowest T_s of the structural $R32 \rightarrow P3_121$ phase transition among iron borates ($T_s = 88 \text{ K}$), and the transition is completely suppressed in $Eu_{0.85}La_{0.15}Fe_3(BO_3)_4$ [29]. This mixed system gives an additional interesting opportunity to explore the possibility of shifting the temperature of a structural PT below the magnetic ordering temperature. Thermodynamic measurements on powder samples of $EuFe_3(BO_3)_4$ revealed an antiferromagnetic ordering, with a well-defined λ -type anomaly in the specific heat vs temperature dependence peaked at $T_N = 34 \text{ K}$ [17]. Magnetic [7,34] and spectroscopic [20,29,35] measurements on $EuFe_3(BO_3)_4$ single crystals confirmed $T_N = 34 \text{ K}$ and showed that the magnetic structure of the Fe magnetic moments is of an easy-plane type. Rare known cases when the temperature of a structural phase transition is lower than the temperature of a magnetic ordering, $T_s < T_N$, refer to temperatures much higher than room temperature [36,37].

We use here the temperature-dependent high-resolution spectroscopy of $f-f$ transitions of the Eu^{3+} ions in $Eu_{1-x}La_xFe_3(BO_3)_4$ mixed crystals to precisely detect phase transitions. Transmission spectra of $EuFe_3(BO_3)_4$ were thoroughly studied earlier in Ref. [29] in different polarizations and in wide spectral (30–200 and 900–23 000 cm^{-1}) and temperature (3.5–300 K) ranges. A complete assignment of spectral lines was performed [29]. In the high-temperature $R32$ structural phase, the crystal field (CF) of D_3 symmetry splits the free Eu^{3+} ion’s levels into Γ_1 and Γ_2 singlets and Γ_3 non-Kramers doublets. In the low-temperature $P3_121$ phase, the symmetry of the Eu^{3+} position lowers to the C_2 symmetry group possessing only one-dimensional irreducible representations, γ_1 and γ_2 . The ground CF state of Eu^{3+} originates from the 7F_0 free-ion level and is the Γ_1 (γ_1) singlet [29]. At T_s , the Γ_3 doublets of the $R32$ phase split, in general, into $\gamma_1 + \gamma_2$ singlets of the $P3_121$ phase, and all CF levels shift due to CF changes. The antiferromagnetic second-order PT in $EuFe_3(BO_3)_4$ at $T_N = 34 \text{ K}$ also causes splitting of the Γ_3 doublets and level shifts [29]. The obtained results on PTs were additionally checked by specific heat measurements.

In this paper, we show that the structural PT in $Eu_{1-x}La_xFe_3(BO_3)_4$ crystals has a rectangular hysteresis loop (this provides the best conditions for the implementation of memory devices and switches), the width ΔT_s of which, together with the transition temperature T_s , can be changed by changing x . To explain these results, we develop a simple analytical model for a weak first-order structural PT, which shows qualitative agreement with the experimental data. In addition, we demonstrate the case $T_s < T_N$ in two members of the $Eu_{1-x}La_xFe_3(BO_3)_4$ series.

II. EXPERIMENT

The $Eu_{1-x}La_xFe_3(BO_3)_4$, $x = 0, 0.05, 0.11, 0.12, 0.15$ single crystals were grown by the solution-melt technique [38] using the Li_2WO_4 -based flux to avoid the impurities of bismuth ions, which enter the crystal in the course of growth from the flux based on $Bi_2Mo_3O_{12}$ [29]. The crystals were

about $3 \times 3 \times 4 \text{ mm}^3$ in size and of good optical quality. The space group, lattice constants, and orientation of the axes in the studied crystals were obtained with a Smart APEXII diffractometer (Mo $K\alpha$, $\lambda = 0.7106 \text{ \AA}$) at room temperature. All the crystals were single phase, possessed the trigonal $R32$ space symmetry group, and had the structure of the huntite mineral [1,2].

X-ray fluorescence (XRF) elemental analysis was performed using a Bruker M1 Mistral micro-XRF spectrometer. An analysis of six points (in an area of about $100 \mu\text{m}$ in size) on the crystal was carried out for specified elements (Eu, La, W) and a correction for the element mass was done, after which the data were averaged. The typical spread in values was no more than 2%. The tungsten in the samples was not detected. The results obtained confirmed with high accuracy the La/Eu concentrations specified during the crystal growth. Several examples on the XRF measurements are given in the Supplemental Material [39].

Elements lighter than Be (as Li) cannot be detected by the XRF method. However, while Bi^{3+} from the $\text{Bi}_2\text{Mo}_3\text{O}_{12}$ flux has the same charge state as the Eu^{3+} ion and a relatively close ionic radius [$r(\text{Bi}^{3+}) = 1.03 \text{ \AA}$, $r(\text{Eu}^{3+}) = 0.947 \text{ \AA}$], Li^+ differs greatly from both Eu^{3+} and Fe^{3+} in these parameters [$r(\text{Li}^+) = 0.76 \text{ \AA}$, $r(\text{Fe}^{3+}) = 0.55 \text{ \AA}$]. The incorporation of lithium into the crystal would lead to a strong local deformation of the lattice near Li in place of Eu and/or Fe and the appearance of oxygen vacancies for charge compensation. In this case, the Eu^{3+} ions located in the vicinity of these defects would experience a perturbed crystal field, which would shift their crystal-field levels. As a result, additional lines in the optical spectra of the Eu^{3+} ions would appear. We clearly observed such lines in the high-resolution spectra of $\text{YbAl}_3(\text{BO}_3)_4$ [40,41] and $\text{EuFe}_3(\text{BO}_3)_4$ [29] grown with the $\text{Bi}_2\text{Mo}_3\text{O}_{12}$ flux, while no traces of any additional lines were found in the spectra of the samples studied in this work.

Samples for optical measurements were cut parallel to the c axis and polished. The 0.1–1 mm thick samples were used for measurements in different spectral regions. Their orientation was additionally checked by optical polarization methods. Far-infrared vibrational spectroscopy measurements with a Bruker IFS 125 HR Fourier spectrometer confirmed that the samples were single phase [42].

Temperature-dependent (3.5–100 K) high-resolution (0.1 cm^{-1}) transmission spectra in the region of $f\text{-}f$ transitions of the Eu^{3+} ions in $\text{Eu}_{1-x}\text{La}_x\text{Fe}_3(\text{BO}_3)_4$ mixed crystals were measured using a Fourier spectrometer, Bruker IFS 125 HR; a closed helium-cycle cryostat, Cryomech ST403; and a dual-sensor temperature control and stabilization system, Lakeshore 335, with silicon diode sensors. In the vicinity of T_s , the temperature was stabilized with a precision of $\pm 5 \text{ mK}$; each point was measured for 1 min and the distance between points was set at 50 mK. Preliminary experiments have shown that there is no change in the hysteresis loops in the cases of fast ($\sim 1 \text{ s}$ per point, with distance between points 100 mK) and slow ($\sim 5 \text{ min}$ per point, with distance between points 50 mK) cooling/heating rates.

Temperature dependences of the specific heat were measured on a PPMS-9 setup manufactured by Quantum Design (USA).

III. EXPERIMENTAL RESULTS

A. Spectroscopic detection of the phase transitions in $\text{Eu}_{1-x}\text{La}_x\text{Fe}_3(\text{BO}_3)_4$

Figure 1 shows the temperature evolution of the Eu^{3+} spectra in the low-frequency range of the ${}^7F_0 \rightarrow {}^7F_5$ infrared optical transition for $\text{Eu}_{1-x}\text{La}_x\text{Fe}_3(\text{BO}_3)_4$ single crystals. In this frequency region, transitions from the ground Γ_1 state to the levels 3825 cm^{-1} (Γ_2), 3831 cm^{-1} (Γ_3), 3854 cm^{-1} (Γ_3), 3903 cm^{-1} (Γ_3), and 3960 cm^{-1} (Γ_3) are present in the $R32$ phase of $\text{EuFe}_3(\text{BO}_3)_4$ [29]. In this parent compound ($x = 0$), at the $R32 \rightarrow P3_121$ structural phase transition temperature $T_s = 87 \text{ K}$, abrupt shifts of these lines ranging from -6 to $+11 \text{ cm}^{-1}$ [29] and marked changes of the intensities are observed. No noticeable splitting of these particular Γ_3 levels has been found at the structural phase transition [see Fig. 1(a)].

Below the temperature of magnetic ordering, at about 30 K, the lowest-frequency $\Gamma_1 \rightarrow \Gamma_2 + \Gamma_3$ line demonstrates a well-observed increasing splitting $\Delta(T)$ reaching 20.3 cm^{-1} at 5 K [see Fig. 1(a)]. This splitting is due to the Eu-Fe exchange interaction and is determined, basically, by the ordering of the iron magnetic moments nearest to a Eu^{3+} ion; it reflects a short-range order in the Fe magnetic subsystem. As a short-range order remains at $T > T_N$, the splitting does not vanish at T_N – a “tail” of residual splitting persists into a paramagnetic region. The tail is more pronounced in low-dimensional systems [43]. The temperature of a magnetic ordering can be determined as the abscissa of the point of inflection in the $\Delta(T)$ curve [44]. In such way, we have found $T_N = 34 \pm 1 \text{ K}$ for our $\text{EuFe}_3(\text{BO}_3)_4$ sample grown with the Li_2WO_4 flux, which is the same value as spectroscopically determined earlier for $\text{EuFe}_3(\text{BO}_3)_4$ crystals grown with the $\text{Bi}_2\text{Mo}_3\text{O}_{12}$ flux [29,35] and is in agreement with $T_N = 34 \text{ K}$ found from the specific heat measurements on powder samples obtained by solid-state synthesis [17]. The splitting of the lowest-frequency line is observed also in the spectra of $\text{Eu}_{0.85}\text{La}_{0.15}\text{Fe}_3(\text{BO}_3)_4$ [see Fig. 1(b)], where the structural PT is suppressed and the magnetic ordering takes place in the $R32$ phase [29]. The same procedure as described above gave the value $T_N = 33 \pm 1 \text{ K}$ for the $\text{Eu}_{0.85}\text{La}_{0.15}\text{Fe}_3(\text{BO}_3)_4$ sample.

Thus, in this spectral region, the $R32 \rightarrow P3_121$ structural PT manifests itself by an abrupt shift of spectral lines but a magnetic ordering causes a splitting of the lowest-frequency line, so that both PTs can be recorded. To additionally check the used spectroscopic method, we have performed specific heat measurements of our samples $\text{EuFe}_3(\text{BO}_3)_4$ and $\text{Eu}_{0.88}\text{La}_{0.12}\text{Fe}_3(\text{BO}_3)_4$. The results are shown in Fig. 2. They confirm applicability of the spectroscopic method.

We note that in the case of the second-order PT that manifests itself by a sharp λ -type anomaly in the specific heat vs temperature dependence the PT temperature can be determined with a better precision than by the spectroscopic method.

B. Decoupled low-temperature structural and magnetic phase transitions in $\text{Eu}_{1-x}\text{La}_x\text{Fe}_3(\text{BO}_3)_4$

In many magnetic compounds also demonstrating a structural PT, the latter occurs simultaneously with a magnetic

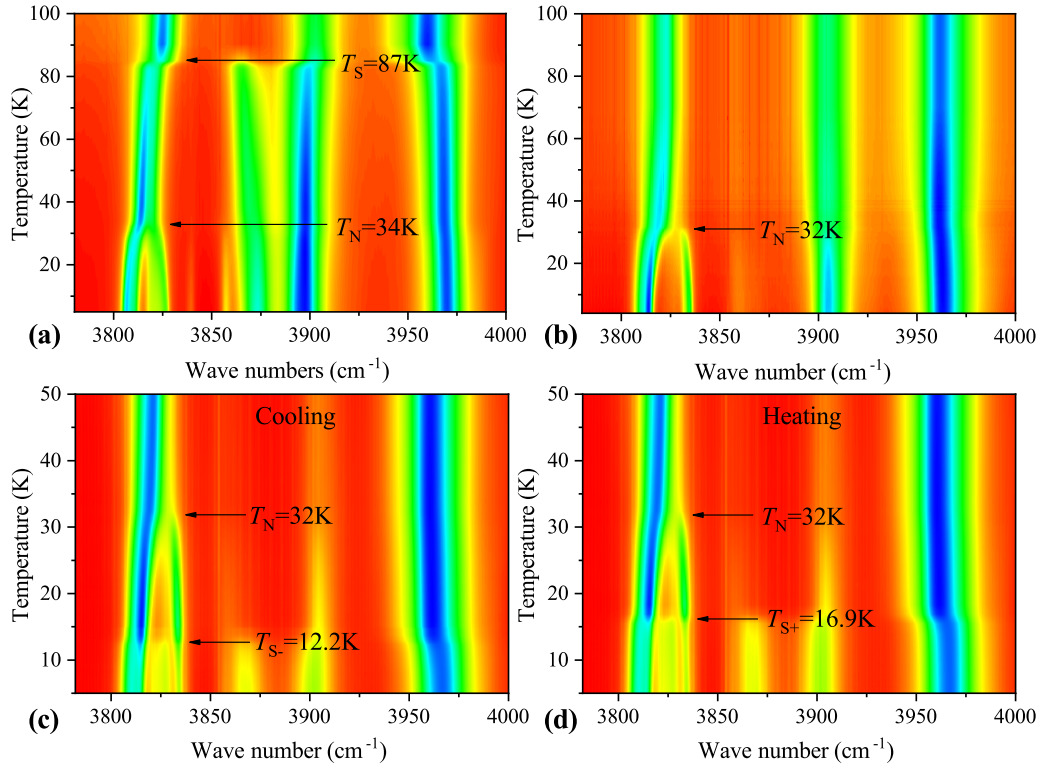


FIG. 1. Intensity maps in the wave number–temperature axes in the region of the ${}^7F_0 \rightarrow {}^7F_5$ transition of Eu^{3+} in (a) $\text{EuFe}_3(\text{BO}_3)_4$, (b) $\text{Eu}_{0.85}\text{La}_{0.15}\text{Fe}_3(\text{BO}_3)_4$, and (c,d) $\text{Eu}_{0.88}\text{La}_{0.12}\text{Fe}_3(\text{BO}_3)_4$ at (c) cooling and (d) heating.

ordering, because of the spin-lattice interactions. Spin-Peierls [45] or spin-Peierls-like [46] compounds and compounds with frustrating (disordering) interactions between magnetic ions

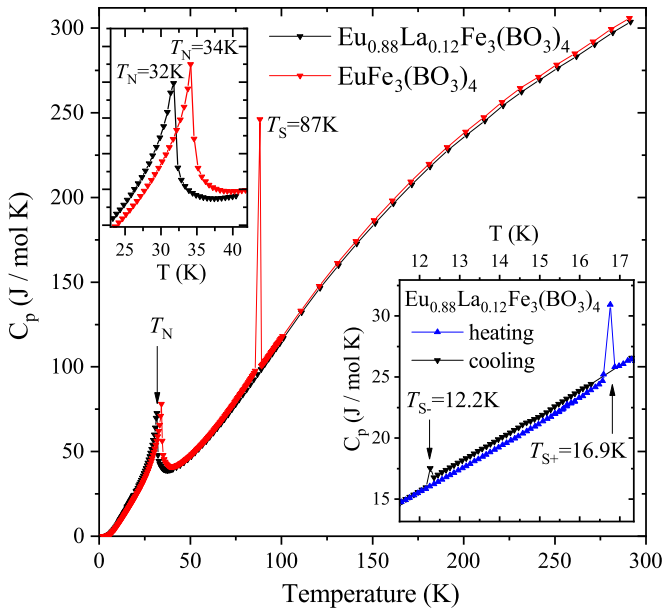


FIG. 2. The temperature dependences of the specific heat of $\text{EuFe}_3(\text{BO}_3)_4$ (red symbols) and $\text{Eu}_{0.88}\text{La}_{0.12}\text{Fe}_3(\text{BO}_3)_4$ (black symbols) single crystals. Upper inset: the region of the magnetic PT for both compounds in an expanded scale. Lower inset: the region of the structural PT in $\text{Eu}_{0.88}\text{La}_{0.12}\text{Fe}_3(\text{BO}_3)_4$ at cooling (black symbols) and heating (blue symbols).

[47–49] can be mentioned as main examples. Decoupled structural and magnetic PTs are also known; however, in a majority of cases, the temperature of a magnetic ordering is lower than the temperature of a structural PT (see, e.g., [50,51]). We are aware of only two cases where the temperature of a structural PT is lower than the temperature of a magnetic ordering, $T_s < T_N$: namely, the case of copper ferrite CuFe_2O_4 with $T_N \approx 750$ K undergoing a PT from the cubic to tetragonal phase at $T_s \approx 660$ K [37] and the case of $\text{Pb}_{1.08}\text{Ba}_{0.92}\text{Fe}_2\text{O}_5$ with $T_N = 625$ K and $T_s = 540$ K corresponding to a second-order PT between two orthorhombic structures, $Imma$ and $Pnma$, possessing the same point group mmm [36]. For the latter compound, it was shown that the magnetic structure does not change through the structural PT. In both cases, the PTs' temperatures are well above room temperature.

In RE iron borates, the temperature of the structural PT is substantially higher than the temperature of magnetic ordering; the difference $T_s - T_N$ scales from 407 K [$\text{YFe}_3(\text{BO}_3)_4$] to 56 K [$\text{EuFe}_3(\text{BO}_3)_4$] [17]. We have shown earlier that in $\text{Eu}_{0.85}\text{La}_{0.15}\text{Fe}_3(\text{BO}_3)_4$ the structural PT is completely suppressed but the temperature of magnetic ordering is the same as in $\text{EuFe}_3(\text{BO}_3)_4$, within the precision of measurements [29]. The question arises: Is it possible to shift T_s below T_N ($0 < T_s < T_N$) by changing the composition of $\text{Eu}_{1-x}\text{La}_x\text{Fe}_3(\text{BO}_3)_4$ single crystals? Because of the multiferroicity of RE iron borates with interacting electron, spin, and lattice degrees of freedom, this is not a trivial question.

We succeeded in observing the structural PT below the Néel temperature T_N in two members of the $\text{Eu}_{1-x}\text{La}_x\text{Fe}_3(\text{BO}_3)_4$ series, namely, in the compounds with

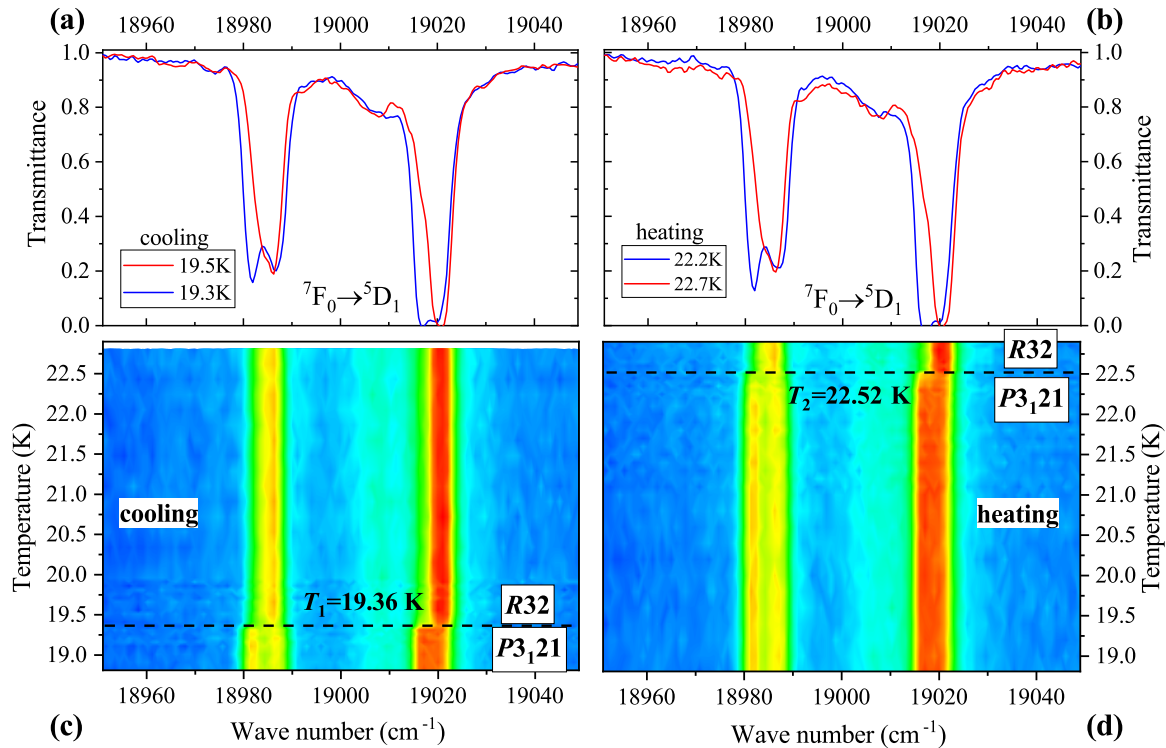


FIG. 3. Temperature-dependent transmission spectra of a 1 mm thick $\text{Eu}_{0.9}\text{La}_{0.11}\text{Fe}_3(\text{BO}_3)_4$ single crystal at (a), (c) cooling and (b), (d) heating. (a), (b) The spectra at two temperatures above and below T_s . (c), (d) The spectra presented as intensity maps in the wave number-temperature axes.

$x = 0.11$ and 0.12 . Figure 1(c) presents the data on the $\text{Eu}_{0.88}\text{La}_{0.12}\text{Fe}_3(\text{BO}_3)_4$ single crystal at cooling. A splitting of the lowest-frequency spectral line manifests a magnetic-ordering second-order PT at $T_N = 33 \pm 1$ K in the $R32$ structural phase of the crystal. The temperature $T_N = 32$ K follows from the specific heat measurements on $\text{Eu}_{0.88}\text{La}_{0.12}\text{Fe}_3(\text{BO}_3)_4$. Specific heat measurements revealed $T_N = 34$ K for $\text{EuFe}_3(\text{BO}_3)_4$ (see Fig. 2, upper inset). The difference of 2 K in magnetic ordering temperatures for $\text{EuFe}_3(\text{BO}_3)_4$ ($T_N = 34$ K, $r = 0.947$ Å) and $\text{Eu}_{0.88}\text{La}_{0.12}\text{Fe}_3(\text{BO}_3)_4$ ($T_N = 32$ K, $r_{\text{eff}} = 0.957$ Å) is in agreement with the $T_N(r)$ dependence [17] (here, $r_{\text{eff}} = 0.88r_{\text{Eu}} + 0.12r_{\text{La}}$ [29]).

With further cooling of the $\text{Eu}_{0.88}\text{La}_{0.12}\text{Fe}_3(\text{BO}_3)_4$ crystal by another 20 K, the $R32 \rightarrow P3_121$ structural PT takes place. The splitting of the lowest-frequency spectral line in Fig. 1(c), which manifests a magnetic-ordering PT, does not change across the structural PT (an additional spectral structure in the low-temperature phase is due to appearance of magnetically nonequivalent positions for RE ions [29]). This is in favor of unchanged magnetic structure. Here, as in the already mentioned case of the $Imma \rightarrow Pnma$ PT in $\text{Pb}_{1.08}\text{Ba}_{0.92}\text{Fe}_2\text{O}_5$, where the magnetic structure was shown to be the same both above and below T_s [36], the point group does not change across the $R32 \rightarrow P3_121$ structural PT [2].

At heating, the $P3_121 \rightarrow R32$ structural PT occurs at a higher temperature (thermal hysteresis) but T_N does not change [see Fig. 1(d), lower inset of Fig. 2].

C. Thermal hysteresis across the structural phase transition in $\text{Eu}_{1-x}\text{La}_x\text{Fe}_3(\text{BO}_3)_4$

To register the thermal hysteresis at the structural PT between the $R32$ and $P3_121$ phases of $\text{Eu}_{1-x}\text{La}_x\text{Fe}_3(\text{BO}_3)_4$ we have chosen the σ -polarized strong absorption line 19019 cm^{-1} in the visible spectral region corresponding to the $\Gamma_1(^7F_0) \rightarrow \Gamma_2(^5D_1)$ optical transition between singlet energy levels of Eu^{3+} in the $R32$ phase of $\text{EuFe}_3(\text{BO}_3)_4$ [29]. Figure 3 displays the temperature-dependent transmission spectra of a 1 mm thick $\text{Eu}_{0.9}\text{La}_{0.11}\text{Fe}_3(\text{BO}_3)_4$ single crystal in the region of this absorption line. The line abruptly shifts and grows in intensity at the temperature T_s of the $R32 \rightarrow P3_121$ structural PT. As a result, the transmittance drops from 0.7 to zero at the wave number of 19016 cm^{-1} . The neighboring line 18987 cm^{-1} , originating from the singlet-doublet optical transition $\Gamma_1(^7F_0) \rightarrow \Gamma_3(^5D_1)$ in the $R32$ phase, splits into two lines in the $P3_121$ phase due to a splitting of the Γ_3 doublet in the C_2 symmetry (see Fig. 3).

Figure 3 clearly demonstrates that the temperature T_s of the structural phase transition (i) can be precisely determined from the spectra and (ii) differs markedly at cooling and heating the sample; i.e., the thermal hysteresis ΔT_s exists. In particular, $\Delta T_s = 3.16$ K in the case of $\text{Eu}_{0.9}\text{La}_{0.11}\text{Fe}_3(\text{BO}_3)_4$. In the temperature region between T_1 and T_2 , the $R32$ and $P3_121$ structural phases do not coexist (see Fig. 3).

Figure 4 shows the thermal hysteresis ΔT_s at the structural phase transition in a pure $\text{EuFe}_3(\text{BO}_3)_4$ single crystal and in a crystal with 12% lanthanum, $\text{Eu}_{0.88}\text{La}_{0.12}\text{Fe}_3(\text{BO}_3)_4$.

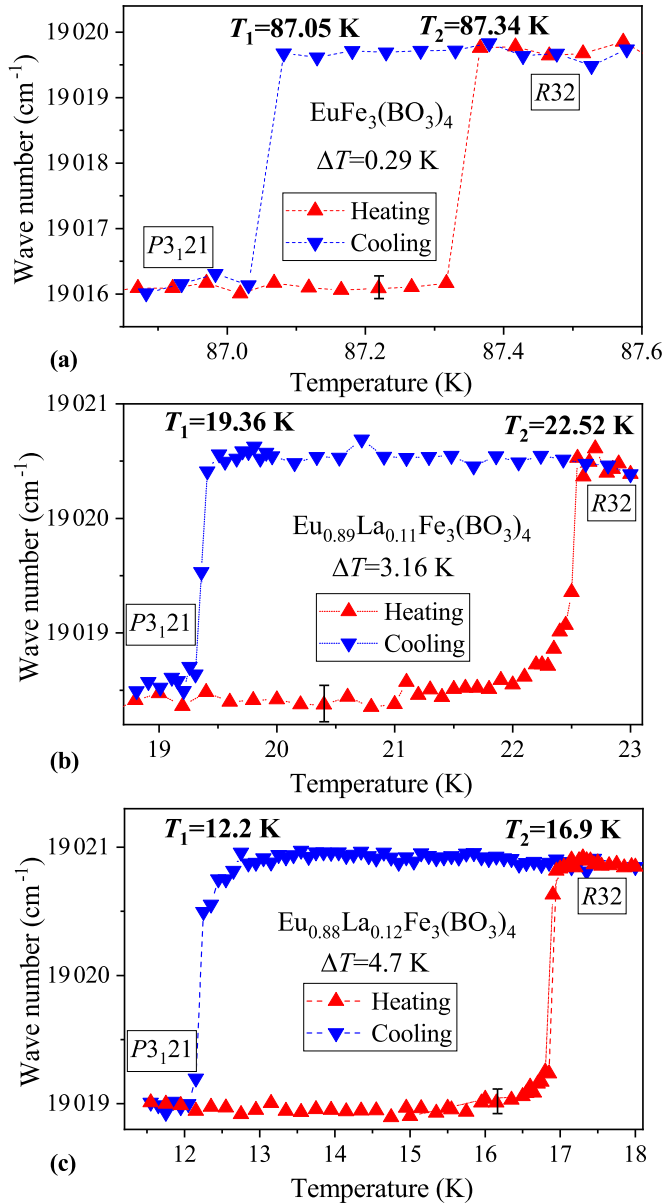


FIG. 4. Position of the $\Gamma_1(^7F_0) \rightarrow \Gamma_2(^5D_1)$ optical transition as a function of temperature at cooling (blue triangles) and heating (red triangles) for (a) $\text{EuFe}_3(\text{BO}_3)_4$, (b) $\text{Eu}_{0.89}\text{La}_{0.11}\text{Fe}_3(\text{BO}_3)_4$, and (c) $\text{Eu}_{0.88}\text{La}_{0.12}\text{Fe}_3(\text{BO}_3)_4$ single crystals.

The position of the considered Eu^{3+} spectral line was measured in a quasistationary mode at cooling and heating the sample. In a pure $\text{EuFe}_3(\text{BO}_3)_4$ crystal, the line's position changes between 19 020 and 19 016 cm^{-1} within ≤ 0.05 K, at $T_1 = 87.05$ K when cooling and at $T_2 = 87.34$ K when heating the sample (the hysteresis is $\Delta T_s = 0.29$ K). In $\text{Eu}_{0.88}\text{La}_{0.12}\text{Fe}_3(\text{BO}_3)_4$, the transition remains very sharp (which testifies to a homogeneous distribution of the lanthanum impurity) but the hysteresis loop is 16 times broader (see Fig. 4).

This nearly rectangular hysteresis loop can be used to implement an optical storage device. The crystal must be cooled below the PT temperature and then heated to enter the hysteresis loop region. Recording can be achieved with a laser pulse

that heats the local area above the PT temperature. Reading is carried out by a weak light beam with a wavelength at which the transmission differs markedly for the two structural phases.

In the following section, we present a simple model that explains the main features of the structural phase transition in $\text{Eu}_{1-x}\text{La}_x\text{Fe}_3(\text{BO}_3)_4$ single crystals and makes it possible to understand the reasons for the increased hysteresis in impurity crystals.

IV. MODEL DESCRIPTION

A. Model of interacting local order parameters

To develop an analytical and intuitively transparent model we assume that the structural instability in a crystal is generated by interactions within a relatively small region of the crystal. Below a certain local critical temperature T_L this instability results in a quasistationary rearrangement of atoms, and this rearrangement can be associated with some local order parameter (LOP) such that $P = P_0(T_L - T)^{1/2}$. The value of LOP is constant over the aforementioned small region [we call it the ‘‘coherent region’’ (CR)], and may randomly change direction (fluctuate), thus recovering the crystal symmetry above T_L . Below T_L it is convenient to represent the entire crystal as consisting of closely packed CRs with LOPs randomly fluctuating in orientation while the ordered state is formed when all LOPs are static and parallel.

It is convenient to take the energy of the ordered state as a reference point, meaning that the inter-LOP interaction is nonzero only in the disordered phase and is assumed to not affect T_L . A suitable function for the interaction energy between neighboring i th and j th LOPs can be taken in the form

$$E_{ij} = \gamma \langle (P_i - P_j)^2 \rangle = 2\gamma(P^2 - \langle P_i P_j \rangle), \quad \langle P_i^2 \rangle = \langle P_j^2 \rangle = P^2, \quad (1)$$

where $\gamma > 0$ is a constant and $\langle \dots \rangle$ means averaging over all possible LOP states. Neighboring LOPs are assumed independent in the disordered phase; therefore $\langle P_i P_j \rangle = 0$ and $E_{ij} = 2\gamma P^2$. In the ordered phase, $\langle P_i P_j \rangle = P^2$ and $E_{ij} = 0$, in agreement with our assumption about the reference state. Independent LOP fluctuations in the disordered phase apparently increase both the system's energy and entropy. Therefore, the phase transition in our model is a result of the trade-off between the inter-LOP interaction energy and the LOP's entropy. The latter for a single LOP, which can occupy M possible states (orientations), is $S = k_B \ln(M)$. Decreasing the crystal temperature below T_L reduces the entropic contribution to free energy and makes it more favorable for LOPs to order into a cluster and become static. Such a cluster can be considered as a nucleus of the new bulk phase—see Fig. 5(a). Similarly, the disordered phase nucleates in the bulk as shown in Fig. 5(b). Hence, we can describe the phase transformation in the system of LOPs as a kind of liquid-solid phase transition with the liquid phase being represented by fluctuating LOPs and the solid one being a macroscopic cluster of identical static LOPs.

A low (high)-temperature phase nucleation probability W can be determined according to classical nucleation theory as $W = Z \exp(-\Delta/k_B T)$, where Z is the Zel'dovich factor and

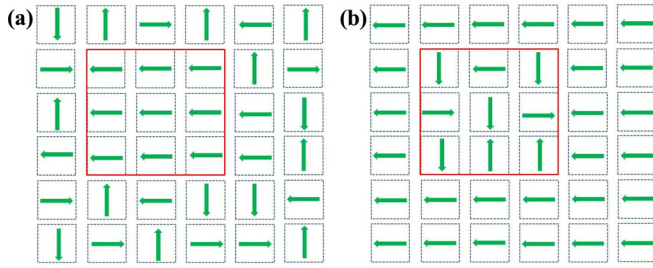


FIG. 5. Schematic representation of phase transformation in the model crystal. (a) Ordered (crystal) phase nucleation in the disordered (liquid) phase; (b) disordered (liquid) phase nucleation in the ordered (crystal) phase.

Δ is the nucleation barrier. For temperature-independent Z the nucleation probability W , and hence the corresponding phase transition temperature in the bulk, T_s (in contrast to the local phase transition temperature T_L), is determined by the value of Δ . It is convenient to define the normalized nucleation barrier $D(\theta) = \Delta/k_B T$ as a function of relative temperature $\theta = T/T_L$. In our model, it is determined by (see the Appendixes)

$$D(\theta) = \frac{0.27}{C\theta} \frac{(1-\theta)}{[C\theta/(1-\theta) - 1]^2}, \quad (2)$$

where $C = 1.8k_B/(6\gamma P_0^2)$. As shown in the Appendixes, Eq. (2) at $\theta < 1/(C+1)$ gives the nucleation barriers for crystallization, and at $\theta > 1/(C+1)$ those for melting. The phase transition temperatures for crystallization and melting fulfill the respective conditions too. To determine particular values of the phase transition temperatures, we assign $D(\theta)$ a certain value, say, 3. Then for each value of C , we determine the crystallization and melting temperatures graphically as illustrated in Fig. 6. They are given by the crossing points of the dotted line with the corresponding solid line in the regions of increasing $D(\theta)$ [$\theta < 1/(C+1)$] and decreasing $D(\theta)$ [$\theta > 1/(C+1)$] for crystallization and melting, respectively. As can be seen from Fig. 6, the parameter C , besides shifting the phase transition temperatures, also significantly affects the thermal hysteresis (difference between the melting and crystallization temperatures).

B. Influence of a substitutional impurity on the PT temperature

The role of substitutional impurity in our model can be taken into account within the mean-field approximation in terms of a change in the local phase transition temperature T_L and the value of P_0 . By analogy with the established linear dependence of T_s on the impurity concentration x [17,19,25,29] we assume that the local phase transition temperature $T_L(x)$ in our model impurity crystal can also be approximated as $T_L(x) = T_L(1 - \alpha x)$ with constant $\alpha > 0$. It is reasonable to expect that the weakening of the structural instability resulting in decreasing $T_L(x)$ also decreases the structural deformation associated with the phase transition; i.e., it decreases the saturation value of the local order parameter $P_0(x)$. In the simplest scenario, such a decrease can be assumed to be linear with x , namely, $P_0(x) = P_0(1 - \beta x)$ with a positive constant β . Substituting the two expressions into Eq. (2), we obtain the

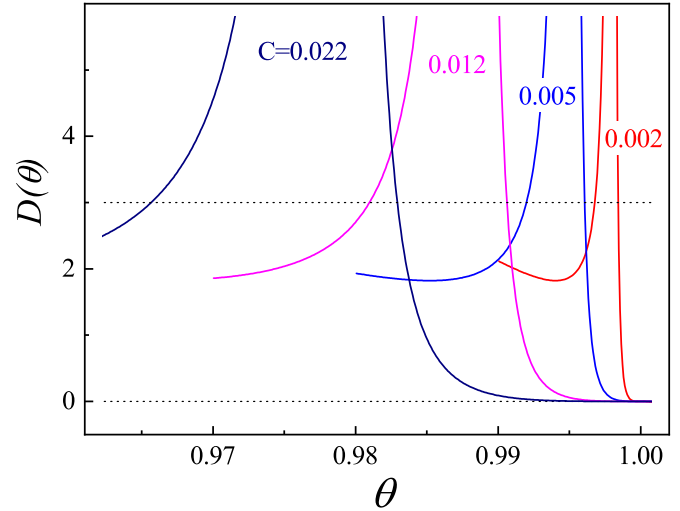


FIG. 6. Nucleation barriers (in $k_B T$ units) for crystallization [left-hand side slopes of the singularity at $C\theta/(1-\theta) = 1$] and melting [right-hand side slopes of the singularity at $C\theta/(1-\theta) = 1$] as functions of reduced temperature $\theta = T/T_L$ calculated using Eq. (2) with the value of parameter C indicated in the figure. Dotted line determines a chosen level of the nucleation barrier that determines (by crossing with solid lines) the corresponding phase transition temperature.

nucleation barrier $D(\theta, x)$ for impurity crystals:

$$D(\theta, x) \approx \frac{0.27}{C\theta} \frac{(1 - \alpha x - \theta)(1 - \beta x)^2}{[1 - C\theta/(1 - \alpha x - \theta)/(1 - \beta x)^2]^2}. \quad (3)$$

This function can be used to approximate experimental results with the fit parameters α and β . The value of C is determined using the value of hysteresis in the pure crystal ($x = 0$).

The nucleation barriers given by Eq. (3) as functions of θ are plotted in Fig. 7 for various impurity concentrations x . A comparison of the phase transition temperatures can be achieved assuming the Zel'dovich factor Z to be a constant and considering the same relative nucleation barrier $D(\theta, x)$ for both heating and cooling at various x . We have chosen $D(\theta, x) = 3$ (dotted line in Fig. 7) to illustrate how well the model describes the observed variation in the phase transition temperature T_B and hysteresis ΔT_B for various impurity concentrations x in $\text{Eu}_{1-x}\text{La}_x\text{Fe}_3(\text{BO}_3)_4$.

It is useful to analyze Eq. (3) in the case $D(\theta) = D_0 \gg 1$ using $C\theta/(1 - \alpha x - \theta)/(1 - \beta x)^2 = 1 + \delta$ with the approximate solutions $\delta \approx \pm \delta_0$, where $\delta_0 = \sqrt{0.27/D_0} \ll 1$. Then, the phase transition temperatures for melting θ_+ and crystallization θ_- and the hysteresis $\Delta\theta = \theta_+ - \theta_-$ can be expressed analytically:

$$\theta_{\pm} = \frac{(1 - \alpha x)(1 \pm \delta_0)(1 - \beta x)^2}{[C + (1 \pm \delta_0)(1 - \beta x)^2]},$$

$$\Delta\theta \approx \frac{2\delta_0 C(1 - \alpha x)(1 - \beta x)^2}{[C + (1 - \beta x)^2]^2}. \quad (4)$$

Taking as before $D_0 = 3$ and the other parameter values as indicated in the caption to Fig. 8, we have found reasonable agreement of our analytical expression for hysteresis (red line

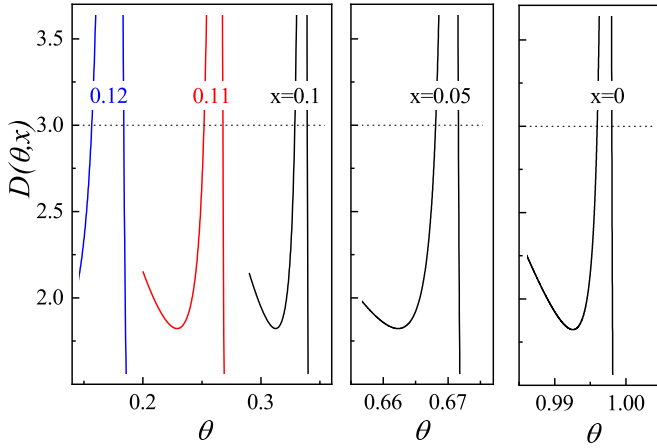


FIG. 7. Nucleation barriers (in $k_B T$ units) for crystallization (left-hand side slopes—see caption to Fig. 6) and melting (right-hand side slopes) as functions of reduced temperature $\theta = T/T_L$ for different impurity concentrations x calculated using Eq. (3) with the model parameters $\alpha = 6.5$, $\beta = 7.5$, and $C = 0.0025$. Dotted line determines a chosen conditional level of the nucleation barrier, hence the temperatures (determined by crossing with solid lines), at which the corresponding phase transition takes place.

in Fig. 8) with the “exact” (graphical) solution (dotted line in Fig. 8). The analytical expression allows also checking of the hysteresis behavior in different situations. For example, if the factor $(1 - \beta x)^2$ accounting for the temperature dependence of the LOP interface energy is set to 1 (no temperature dependence), the hysteresis expression [Eq. (4)] reduces to $\Delta\theta \approx 2\delta_0 C(1 - \alpha x)/(C + 1)^2$, predicting a linear decrease

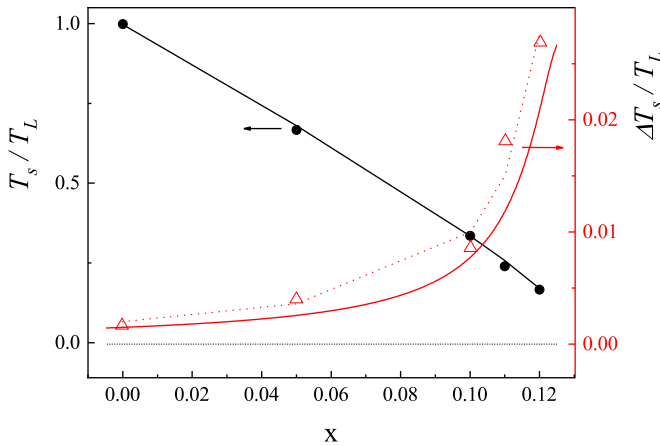


FIG. 8. Average experimental phase transition temperature in the bulk $T_s = 0.5(T_{s,\text{heat}} + T_{s,\text{cool}})$ (black symbols) and the hysteresis $\Delta T_s = (T_{s,\text{heat}} - T_{s,\text{cool}})$ (red symbols), both normalized on the value of $T_L = 87$ K, as functions of impurity atom concentration x in $\text{Eu}_{1-x}\text{La}_x\text{Fe}_3(\text{BO}_3)_4$ single crystals. For the T_L value we used the structural phase transition temperature in the pure $\text{EuLaFe}_3(\text{BO}_3)_4$ single crystal. Black solid and red dotted lines are model calculations with the parameter values $\alpha = 6.5$, $\beta = 7.5$, and $C = 0.0025$ obtained for the relative nucleation barriers $\Delta/k_B T = 3$ as illustrated in Fig. 7. The red solid line is given by the expression Eq. (4) with $\alpha = 6.5$, $\beta = 0$, and $C = 0.0025$. The value of C was calculated using the experimental value of hysteresis at $x = 0$.

with increasing x . The almost linear decrease in thermal hysteresis has been experimentally detected for ferroelectric phase transition in mixed $\text{Ba}_{1-x}\text{Sr}_x\text{TiO}_3$ crystals [52]. This fact indicates the significant potential of our model for interpreting the features of phase transition in different materials.

V. CONCLUSION

We have performed detailed spectroscopic studies of structural phase transformation in mixed single crystals $\text{Eu}_{1-x}\text{La}_x\text{Fe}_3(\text{BO}_3)_4$, which allowed us to determine both the transition temperature T_s and the value of thermal hysteresis ΔT_s for different compositions. We show that the composition variation in the range $0 \leq x \leq 0.12$ allows the shifting of T_s from 87 K down to ~ 12 K, simultaneously increasing ΔT_s from 0.3 K up to 4.7 K. An almost rectangular hysteresis loop observed at the structural PT in $\text{Eu}_{1-x}\text{La}_x\text{Fe}_3(\text{BO}_3)_4$ crystals is favorable for the implementation of switches and optical memory devices operating at low temperatures used, in particular, in quantum technologies. Other mixed $R_{1-x}R'_x\text{Fe}_3(\text{BO}_3)_4$ (where R and R' are RE elements) can provide the temperatures of the structural PT up to 450 K.

The experimental observations concerning T_s and ΔT_s in the $\text{Eu}_{1-x}\text{La}_x\text{Fe}_3(\text{BO}_3)_4$ solid solutions are described within the developed analytical model of phase transformations of mixed first- to second-order type. The model makes it possible to interpret the observed characteristics of the phase transition in terms of interaction between the local order parameters, and indicates its potential applicability to phase transformations in other materials.

It is found that the observed changes in the structural phase transition parameters do not affect the magnetic phase transformation in this material. Change of T_N from 34 K for $\text{EuFe}_3(\text{BO}_3)_4$ to 32 K for $\text{Eu}_{0.88}\text{La}_{0.12}\text{Fe}_3(\text{BO}_3)_4$ is in agreement with the $T_N(r_{\text{eff}})$ dependence, where $r_{\text{eff}} = (1 - x)r_{\text{Eu}} + xr_{\text{La}}$ for $\text{Eu}_{1-x}\text{La}_x\text{Fe}_3(\text{BO}_3)_4$ (here, r_{Eu} and r_{La} are the ionic radii of Eu^{3+} and La^{3+} , respectively). $\text{Eu}_{0.88}\text{La}_{0.12}\text{Fe}_3(\text{BO}_3)_4$ demonstrates the structural PT at about 12 K, i.e., below the Néel temperature $T_N = 32$ K. This observation of the temperature of the structural phase transition below the temperature of magnetic ordering in the cryogenic temperature range opens up prospects for applications in quantum technologies.

ACKNOWLEDGMENT

This work is supported by the Russian Science Foundation under Grant No. 19-12-00413.

APPENDIX A: NUCLEATION BARRIER FOR CRYSTALLIZATION

Free energy for the system consisting of N LOPs can be expressed in terms of the local order parameter (LOP) P and an interaction constant γ . The latter reflects interaction between the neighboring LOPs averaged over the entire system and attributed to a single LOP. Within this approximation the free energies for the disordered F_{dis} and ordered F_{ord} phases are

$$F_{\text{dis}} = NE_{\text{LOP}} + 6N\gamma P^2 - Nk_B T \ln M, \quad F_{\text{ord}} = NE_{\text{LOP}}, \quad (\text{A1})$$

where E_{LOP} is the LOP bulk energy; γP^2 is the interface energy per LOP for CR of cubic shape. The entropy term in Eq. (A1) arises from the multiplicity N_S (the number of

microstates with the same energy) of the disordered state of the LOPs. In the approximation of uncorrelated LOPs (in the disordered state) we can write for the multiplicity of the system containing N LOPs $N_S = M^N$, where M is the number of possible orientations of a single LOP. Defining the entropy as $S = -k_B \ln(N_S) = -k_B N \ln(M)$ one obtains the term in Eq. (A1). If we choose F_{ord} as a reference state, i.e., $F_{\text{ord}} \equiv 0$, then Eq. (A1) reduces down to

$$F_{\text{dis}} = 6N\gamma P^2 - Nk_B T \ln M, \quad F_{\text{ord}} = 0. \quad (\text{A2})$$

The phase transition between disordered and ordered phases starts with the formation of the critical nucleus. For the cubic shape of the critical nucleus containing n LOPs the associated excess free energy is

$$\begin{aligned} \Delta F_{\text{cr}} &= 6\gamma P^2(N - n + n^{2/3}) - (N - n)k_B T \ln M \\ &\quad - \gamma P^2 6N + Nk_B T \ln M \\ &= -6\gamma P^2 n + 6\gamma P^2 n^{2/3} + nk_B T \ln M, \end{aligned} \quad (\text{A3})$$

where $n^{1/3}$ is the side of the critical nucleus. Here we assumed that the interface energy between adjacent LOPs is the same whether both or just one LOP is fluctuating. The size n of the critical nucleus corresponds to the maximum of the excess free energy such that

$$\begin{aligned} \frac{d\Delta F_{\text{cr}}}{dn} &= -6\gamma P^2 + 4\gamma P^2 n^{-1/3} + k_B T \ln M = 0, \\ n &= \frac{(4\gamma P^2)^3}{(6\gamma P^2 - k_B T \ln M)^3}, \quad 6\gamma P^2 > k_B T \ln M. \end{aligned} \quad (\text{A4})$$

We can check that the determined n indeed corresponds to the maximum of ΔF_{cr} :

$$\frac{d^2 \Delta F_{\text{cr}}}{dn^2} = -\frac{4}{3}\gamma P^2 n^{-4/3} = -\frac{4}{3}\gamma P^2 \frac{(6\gamma P^2 - k_B T \ln M)^4}{(4\gamma P^2)^4} < 0.$$

Substituting n from Eq. (A4) and $P = P_0(T_L - T)^{1/2}$ into Eq. (A3) and assuming $M = 6$ (cubic structure above T_L), we obtain the normalized nucleation barrier for crystallization $D_{\text{cr}}(\theta = T/T_L)$,

$$\begin{aligned} D_{\text{cr}}(\theta) &= \frac{\Delta F_{\text{cr}}}{k_B T} = \frac{1}{2} \frac{(4\gamma P^2)^3}{(6\gamma P^2 - k_B T \ln M)^2} \\ &= \frac{0.27}{C\theta} \frac{(1 - \theta)}{[1 - C\theta/(1 - \theta)]^2}, \end{aligned} \quad (\text{A5})$$

where $C = 1.8k_B/(6\gamma P_0^2) < (1 - \theta)/\theta$.

APPENDIX B: NUCLEATION BARRIER FOR MELTING

As the free energy of the crystalline state is taken to be zero we can write ΔF_{mel} assuming that n is now the number

of LOPs in a molten cluster of cubic shape

$$\Delta F_{\text{mel}} = \gamma P^2 6(n + n^{2/3}) - nk_B T \ln M. \quad (\text{B1})$$

Determine the critical value of n :

$$\begin{aligned} \frac{d\Delta F_{\text{mel}}}{dn} &= \gamma P^2(6 + 4n^{-1/3}) - k_B T \ln M = 0, \\ n &= \frac{(4\gamma P^2)^3}{(k_B T \ln M - 6\gamma P^2)^3}, \quad 6\gamma P^2 < k_B T \ln M. \end{aligned} \quad (\text{B2})$$

Substituting it into Eq. (B1) we obtain the relative nucleation barrier for melting,

$$\begin{aligned} D_{\text{mel}}(\theta) &= \frac{\Delta F_{\text{mel}}}{k_B T} = \frac{1}{2} \frac{(4\gamma P^2)^3}{(k_B T \ln M - 6\gamma P^2)^2} \\ &= \frac{0.27}{C\theta} \frac{(1 - \theta)}{(C\theta/(1 - \theta) - 1)^2}, \end{aligned} \quad (\text{B3})$$

where $C = 1.8k_B/(6\gamma P_0^2) > (1 - \theta)/\theta$. As we see, both nucleation barriers given by Eqs. (A5) and (B3) are determined by one and the same expression,

$$D(\theta) = \frac{0.27}{C\theta} \frac{(1 - \theta)}{[C\theta/(1 - \theta) - 1]^2}, \quad (\text{B4})$$

which for $\theta < 1/(C + 1)$ gives the nucleation barriers for crystallization, $D_{\text{cr}}(\theta)$, and for $\theta > 1/(C + 1)$ it gives the nucleation barriers for melting, $D_{\text{mel}}(\theta)$. As a consequence the phase transition temperatures for crystallization and melting fulfill the same conditions accordingly. It is worth noting that the nucleation barrier is determined virtually by the ratio of the energy associated with the LOP entropy to the interface energy per LOP.

The value of C , according to Fig. 7, determines the value of thermal hysteresis for the phase transition under consideration. It is worth pointing out that the hysteresis in our model tends to 0 if $C \rightarrow 0$, meaning that the true second-order phase transition can be reached only as an extreme case. This extreme, however, is due to the approximations used in deriving the model. In a more realistic scenario one would have to consider fluctuations of both the direction and the value of the local order parameter in the vicinity of T_L . It can be shown that these fluctuations would result in zero hysteresis at a nonzero value of the parameter C . Another important approximation of our model is about the constant size of the coherent regions (CRs) carrying the LOPs. This assumption is actually about the constant value of the parameter γ determining the interface energy between the LOPs. A noticeable change in the CR size in the proximity to the second-order phase transition point could affect the C value [see the line below Eqs. (A5) and (B3)] and in a more rigorous treatment should be taken into account together with the order parameter fluctuations.

- [1] N. I. Leonyuk and L. I. Leonyuk, Growth and characterization of $RM_3(\text{BO}_3)_4$ crystals, *Prog. Cryst. Growth Charact. Mater.* **31**, 179 (1995).
 [2] S. A. Klimin, D. Fausti, A. Meetsma, L. N. Bezmaternykh, P. H. M. van Loosdrecht, and T. T. M. Palstra, Evidence for

differentiation in the iron-helical chain in $\text{GdFe}_3(\text{BO}_3)_4$, *Acta Crystallogr., Sect. B* **61**, 481 (2005).

- [3] D. Xue, K. Betzler, H. Hesse, and D. Lammers, Nonlinear optical properties of borate crystals, *Solid State Commun.* **114**, 21 (2000).

- [4] S. Ilas, P. Loiseau, G. Aka, and T. Taira, 240 kW peak power at 266 nm in nonlinear $\text{YAl}_3(\text{BO}_3)_4$ single crystal, *Opt. Express* **22**, 30325 (2014).
- [5] N. N. Kuz'min, K. N. Boldyrev, N. I. Leonyuk, S. Yu. Stefanovich, and M. N. Popova, Luminescence and nonlinear optical properties of borates $\text{LnGa}_3(\text{BO}_3)_4$ ($\text{Ln} = \text{Nd}, \text{Sm}, \text{Tb}, \text{Er}, \text{Dy}, \text{or Ho}$), *Opt. Spectrosc.* **127**, 107 (2019).
- [6] A. Benayas, D. Jaque, J. García Solé, N. I. Leonyuk, E. Bovero, E. Cavalli, and M. Bettinelli, Effects of neodymium incorporation on the structural and luminescence properties of the $\text{YAl}_3(\text{BO}_3)_4$ – $\text{NdAl}_3(\text{BO}_3)_4$ system, *J. Phys.: Condens. Matter* **19**, 246204 (2007).
- [7] A. M. Kadomtseva, Yu. F. Popov, G. P. Vorob'ev, A. P. Pyatakov, S. S. Krotov, K. I. Kamilov, V. Yu. Ivanov, A. A. Mukhin, A. K. Zvezdin, A. M. Kuz'menko, L. N. Bezmaternykh, I. A. Gudim, and V. L. Temerov, Magnetolectric and magnetoelastic properties of rare-earth ferrobates, *Low Temp. Phys.* **36**, 511 (2010).
- [8] R. P. Chaudhury, F. Yen, B. Lorenz, Y. Y. Sun, L. N. Bezmaternykh, V. L. Temerov, and C. W. Chu, Magnetolectric effect and spontaneous polarization in $\text{HoFe}_3(\text{BO}_3)_4$ and $\text{Ho}_{0.5}\text{Nd}_{0.5}\text{Fe}_3(\text{BO}_3)_4$, *Phys. Rev. B* **80**, 104424 (2009).
- [9] T. Kurumaji, K. Ohgushi, and Y. Tokura, Magnetolectric responses from the respective magnetic R and Fe subsystems in the noncentrosymmetric antiferromagnets $R\text{Fe}_3(\text{BO}_3)_4$ ($R = \text{Eu}, \text{Gd}, \text{and Tb}$), *Phys. Rev. B* **89**, 195126 (2014).
- [10] K.-C. Liang, R. P. Chaudhury, B. Lorenz, Y. Y. Sun, L. N. Bezmaternykh, V. L. Temerov, and C. W. Chu, Giant magnetolectric effect in $\text{HoAl}_3(\text{BO}_3)_4$, *Phys. Rev. B* **83**, 180417(R) (2011).
- [11] N. V. Volkov, I. A. Gudim, E. V. Eremin, A. I. Begunov, A. A. Demidov, and K. N. Boldyrev, Magnetization, magnetolectric polarization, and specific heat of $\text{HoGa}_3(\text{BO}_3)_4$, *JETP Lett.* **99**, 67 (2014).
- [12] A. K. Zvezdin, A. M. Kadomtseva, Yu. F. Popov, G. P. Vorob'ev, A. P. Pyatakov, V. Yu. Ivanov, A. M. Kuz'menko, A. A. Mukhin, L. N. Bezmaternykh, and I. A. Gudim, Magnetic anisotropy and magnetolectric properties of $\text{Tb}_{1-x}\text{Er}_x\text{Fe}_3(\text{BO}_3)_4$ ferrobates, *J. Exp. Theor. Phys.* **109**, 68 (2009).
- [13] A. M. Kadomtseva, Yu. F. Popov, G. P. Vorob'ev, N. V. Kostyuchenko, A. I. Popov, A. A. Mukhin, V. Yu. Ivanov, L. N. Bezmaternykh, I. A. Gudim, V. L. Temerov, A. P. Pyatakov, and A. K. Zvezdin, High-temperature magnetolectricity of terbium aluminum borate: The role of excited states of the rare-earth ion, *Phys. Rev. B* **89**, 014418 (2014).
- [14] E. Bovero, Z. D. Luo, Y. D. Huang, A. Benayas, and D. Jaque, Single longitudinal mode laser oscillation from a neodymium aluminium borate stoichiometric crystal, *Appl. Phys. Lett.* **87**, 211108 (2005).
- [15] J. Huang, Y. Chen, X. Gong, Y. Lin, Z. Luo, and Y. Huang, Efficient 1.55 μm laser operation of Er^{3+} in stoichiometric $\text{Sr}_3\text{Yb}(\text{BO}_3)_3$ crystal, *Opt. Mater. Express* **5**, 1579 (2015).
- [16] K. N. Gorbachenya, V. E. Kisel, A. S. Yasukevich, V. V. Maltsev, N. I. Leonyuk, and N. V. Kuleshov, Eye-safe 1.55 μm passively Q -switched $\text{Er}, \text{Yb} : \text{GdAl}_3(\text{BO}_3)_4$ diode-pumped laser, *Opt. Lett.* **41**, 918 (2016).
- [17] Y. Hinatsu, Y. Doi, K. Ito, M. Wakeshima, and A. Alemi, Magnetic and calorimetric studies on rare-earth iron borates $\text{LnFe}_3(\text{BO}_3)_4$ ($\text{Ln} = \text{Y}, \text{La-Nd}, \text{Sm-Ho}$), *J. Solid State Chem.* **172**, 438 (2003).
- [18] M. N. Popova, T. N. Stanislavchuk, B. Z. Malkin, and L. N. Bezmaternykh, Phase transitions and crystal-field and exchange interactions in $\text{TbFe}_3(\text{BO}_3)_4$ as seen via optical spectroscopy, *J. Phys.: Condens. Matter* **24**, 196002 (2012).
- [19] S. A. Klimin, A. B. Kuzmenko, M. A. Kashchenko, and M. N. Popova, Infrared study of lattice dynamics and spin-phonon and electron-phonon interactions in multiferroic $\text{TbFe}_3(\text{BO}_3)_4$ and $\text{GdFe}_3(\text{BO}_3)_4$, *Phys. Rev. B* **93**, 054304 (2016).
- [20] M. N. Popova, Optical spectroscopy of low-dimensional rare-earth iron borates, *J. Magn. Magn. Mater.* **321**, 716 (2009).
- [21] M. N. Popova, E. P. Chukalina, D. S. Erofeev, A. Jablunovskis, I. A. Gudim, and B. Z. Malkin, High-resolution optical spectroscopy and modeling of spectral and magnetic properties of multiferroic $\text{ErFe}_3(\text{BO}_3)_4$, *Phys. Rev. B* **101**, 205108 (2020).
- [22] R. Z. Levitin, E. A. Popova, R. M. Chtsherbov, A. N. Vasiliev, M. N. Popova, E. P. Chukalina, S. A. Klimin, P. H. M. van Loosdrecht, D. Fausti, and L. N. Bezmaternykh, Cascade of phase transitions in $\text{GdFe}_3(\text{BO}_3)_4$, *JETP Lett.* **79**, 423 (2004).
- [23] D. Fausti, A. Nugroho, P. H. M. van Loosdrecht, S. A. Klimin, M. N. Popova, and L. N. Bezmaternykh, Raman scattering from phonons and magnons in $R\text{Fe}_3(\text{BO}_3)_4$, *Phys. Rev. B* **74**, 024403 (2006).
- [24] E. S. Smirnova, O. A. Alekseeva, A. P. Dudka, V. V. Artemov, Y. V. Zubavichus, I. A. Gudim, L. N. Bezmaternykh, K. V. Frolov, and I. S. Lyubutin, Crystal structure, phase transition and structural deformations in iron borate $(\text{Y}_{0.95}\text{Bi}_{0.05})\text{Fe}_3(\text{BO}_3)_4$ in the temperature range 90–500 K, *Acta Crystallogr., Sect. B* **74**, 226 (2018).
- [25] E. S. Smirnova, O. A. Alekseeva, A. P. Dudka, D. N. Khmel'nenin, K. V. Frolov, M. V. Lyubutina, I. A. Gudim, and I. S. Lyubutin, Crystal structure and structural phase transition in bismuth-containing $\text{HoFe}_3(\text{BO}_3)_4$ in the temperature range 11–500 K, *Acta Crystallogr., Sect. B* **75**, 954 (2019).
- [26] U. Adem, L. Wang, D. Fausti, W. Schottenhamel, P. H. M. van Loosdrecht, A. Vasiliev, L. N. Bezmaternykh, B. Büchner, C. Hess, and R. Klingeler, Magnetodielectric and magnetoelastic coupling in $\text{TbFe}_3(\text{BO}_3)_4$, *Phys. Rev. B* **82**, 064406 (2010).
- [27] D. A. Erofeev, E. P. Chukalina, L. N. Bezmaternykh, I. A. Gudim, and M. N. Popova, High-resolution spectroscopy of $\text{HoFe}_3(\text{BO}_3)_4$ crystal: A study of phase transitions, *Opt. Spectrosc.* **120**, 558 (2016).
- [28] T. Usui, Y. Tanaka, H. Nakajima, M. Taguchi, A. Chainani, M. Oura, S. Shin, N. Katayama, H. Sawa, Y. Wakabayashi, and T. Kimura, Observation of quadrupole helix chirality and its domain structure in $\text{DyFe}_3(\text{BO}_3)_4$, *Nat. Mater.* **13**, 611 (2014).
- [29] M. N. Popova, B. Z. Malkin, K. N. Boldyrev, T. N. Stanislavchuk, D. A. Erofeev, V. L. Temerov, and I. A. Gudim, Evidence for a collinear easy-plane magnetic structure of multiferroic $\text{EuFe}_3(\text{BO}_3)_4$: Spectroscopic and theoretical studies, *Phys. Rev. B* **94**, 184418 (2016).
- [30] R. D. Shannon, Revised effective ionic radii and systematic studies of interatomic distances in halides and chalcogenides, *Acta Crystallogr., Sect. A* **32**, 751 (1976).
- [31] H. F. Hamann, M. O'Boyle, Y. C. Martin, M. Rooks, and H. K. Wickramasinghe, Ultra-high-density phase-change storage and memory, *Nat. Mater.* **5**, 383 (2006).

- [32] B. F. Soares, F. Jonsson, and N. I. Zheludev, All-Optical Phase-Change Memory in a Single Gallium Nanoparticle, *Phys. Rev. Lett.* **98**, 153905 (2007).
- [33] A. I. Denisyuk, K. F. MacDonald, F. J. García de Abajo, and N. I. Zheludev, Towards femtojoule nanoparticle phase-change memory, *Jpn. J. Appl. Phys.* **48**, 03A065 (2009).
- [34] V. P. Dyakonov, R. Szymczak, A. D. Prokhorov, E. Zubov, A. A. Prokhorov, G. Petrákovskii, L. Bezmaternikh, M. Berkowski, V. Varyukhin, and H. Szymczak, Magnetic and EPR studies of the $\text{EuFe}_3(\text{BO}_3)_4$ single crystal, *Eur. Phys. J. B* **78**, 291 (2010).
- [35] K. N. Boldyrev, T. N. Stanislavchuk, S. A. Klimin, M. N. Popova, and L. N. Bezmaternikh, Terahertz spectroscopy of multiferroic $\text{EuFe}_3(\text{BO}_3)_4$, *Phys. Lett. A* **376**, 2562 (2012).
- [36] I. V. Nikolaev, H. D'Hondt, A. M. Abakumov, J. Hadermann, A. M. Balagurov, I. A. Bobrikov, D. V. Sheptyakov, V. Yu. Pomjakushin, K. V. Pokholok, D. S. Filimonov, G. Van Tendeloo, and E. V. Antipov, Crystal structure, phase transition, and magnetic ordering in perovskitelike $\text{Pb}_{2-x}\text{Ba}_x\text{Fe}_2\text{O}_5$ solid solutions, *Phys. Rev. B* **78**, 024426 (2008).
- [37] A. M. Balagurov, I. A. Bobrikov, V. Yu. Pomjakushin, D. V. Sheptyakov, and V. Yu. Yushankhai, Interplay between structural and magnetic phase transitions in copper ferrite studied with high-resolution neutron diffraction, *J. Magn. Magn. Mater.* **374**, 591 (2015).
- [38] I. A. Gudim, E. V. Eremin, and V. L. Temerov, Flux growth and spin reorientation in trigonal $\text{Nd}_{1-x}\text{Dy}_x\text{Fe}_3(\text{BO}_3)_4$ single crystals, *J. Cryst. Growth* **312**, 2427 (2010).
- [39] See Supplemental Material at <http://link.aps.org/supplemental/10.1103/PhysRevMaterials.5.094414> for the x-ray fluorescence measurements on $\text{Eu}_{1-x}\text{La}_x\text{Fe}_3(\text{BO}_3)_4$ single crystals.
- [40] M. N. Popova, K. N. Boldyrev, P. O. Petit, B. Viana, and L. N. Bezmaternikh, High-resolution spectroscopy of $\text{YbAl}_3(\text{BO}_3)_4$ stoichiometric nonlinear laser crystals, *J. Phys.: Condens. Matter* **20**, 455210 (2008).
- [41] K. N. Boldyrev, M. N. Popova, M. Bettinelli, V. L. Temerov, I. A. Gudim, L. N. Bezmaternikh, P. Loiseau, G. Aka, and N. I. Leonyuk, Quality of the rare earth aluminum borate crystals for laser applications, probed by high-resolution spectroscopy of the Yb^{3+} ion, *Opt. Mater.* **34**, 1885 (2012).
- [42] E. Yu. Borovikova, K. N. Boldyrev, S. M. Aksenov, E. A. Dobretsova, V. S. Kurazhkovskaya, N. I. Leonyuk, A. E. Savon, D. V. Deyneko, and D. A. Ksenofontov, Crystal growth, structure, infrared spectroscopy, and luminescent properties of rare-earth gallium borates $R\text{Ga}_3(\text{BO}_3)_4$, $R = \text{Nd}, \text{Sm}-\text{Er}, \text{Y}$, *Opt. Mater.* **49**, 304 (2015).
- [43] L. J. de Jongh and A. R. Miedema, Experiments on simple magnetic model systems, *Adv. Phys.* **23**, 1 (1974).
- [44] M. N. Popova, High-resolution spectroscopy of rare earth cuprates and nickelates, *J. Alloys Compd.* **275-277**, 142 (1998).
- [45] M. Hase, I. Terasaki, and K. Uchinokura, Observation of the Spin-Peierls Transition in Linear Cu^{2+} (Spin-1/2) Chains in an Inorganic Compound CuGeO_3 , *Phys. Rev. Lett.* **70**, 3651 (1993).
- [46] M. Isobe, and Y. Ueda, Magnetic susceptibility of quasi-one-dimensional compound $\alpha'\text{-NaV}_2\text{O}_5$ —possible spin-Peierls compound with high critical temperature of 34 K, *J. Phys. Soc. Jpn.* **65**, 1178 (1996).
- [47] S. Li, C. de la Cruz, Q. Huang, Y. Chen, J. W. Lynn, J. Hu, Y. L. Huang, F. Ch. Hsu, K. W. Yeh, M. K. Wu, and P. Dai, First-order magnetic and structural phase transitions in $\text{Fe}_{1+y}\text{Se}_x\text{Te}_{1-x}$, *Phys. Rev. B* **79**, 054503 (2009).
- [48] R. V. Pisarev, M. A. Prosnikov, V. Yu. Davydov, A. N. Smirnov, E. M. Roginskii, K. N. Boldyrev, A. D. Molchanova, M. N. Popova, M. B. Smirnov, and V. Yu. Kazimirov, Lattice dynamics and a magnetic-structural phase transition in the nickel orthoborate $\text{Ni}_3(\text{BO}_3)_2$, *Phys. Rev. B* **93**, 134306 (2016).
- [49] J. Warmuth, M. Bremholm, Ph. Hofmann, J. Wiebe, and R. Wiesendanger, Domain imaging across the magneto-structural phase transitions in Fe_{1+y}Te , *npj Quantum Mater.* **3**, 21 (2018).
- [50] B. F. Alfonso, C. Trobajo, C. Piqué, M. T. Fernández-Díaz, J. R. Fernández, M. A. Salvadó, P. Pertierra, S. García-Granda, J. R. García, and J. A. Blanco, Decoupled structural and non-collinear magnetic phase transitions in $\text{Fe}(\text{ND}_3)_2\text{PO}_4$, *Acta Mater.* **58**, 1741 (2010).
- [51] L. D. Sanjeewa, V. O. Garlea, M. A. McGuire, M. Frontzek, C. D. McMillen, K. Fulle, and J. W. Kolis, Investigation of a structural phase transition and magnetic structure of $\text{Na}_2\text{BaFe}(\text{VO}_4)_2$: A triangular magnetic lattice with a ferromagnetic ground state, *Inorg. Chem.* **56**, 14842 (2017).
- [52] V. V. Lemanov, E. P. Smirnova, P. P. Syrnikov, and E. A. Tarakanov, Phase transitions and glasslike behavior in $\text{Sr}_{1-x}\text{Ba}_x\text{TiO}_3$, *Phys. Rev. B* **54**, 3151 (1996).